MeV Ion Jets from Short-Pulse-Laser Interaction with Thin Foils

M. Hegelich,[1,2] S. Karsch,[1,2] G. Pretzler,[1,2] D. Habs,[2] K. Witte,[1] W. Guenther,[3] M. Allen,[4] A. Blazevic,[5] J. Fuchs,[6] J. C. Gauthier,[6] M. Geissel,[5] P. Audebert,[6] T. Cowan,[4] and M. Roth[5]

[1]*MPI für Quantenoptik, 85748 Garching, Germany*
[2]*Universität München, 85748 Garching, Germany*
[3]*Universität Siegen, 57068 Siegen, Germany*
[4]*General Atomics, San Diego, California 92121*
[5]*GSI Laboratory, 64291 Darmstadt, Germany*
[6]*LULI, Ecole Polytechnique, 91128 Palaiseau, France*

(Received 27 December 2001; published 2 August 2002)

Collimated jets of carbon and fluorine ions up to 5 MeV/nucleon ($\sim$100 MeV) are observed from the rear surface of thin foils irradiated with laser intensities of up to 5×10^{19} W/cm^2. The normally dominant proton acceleration could be surpressed by removing the hydrocarbon contaminants by resistive heating. This inhibits screening effects and permits effective energy transfer and acceleration of other ion species. The acceleration dynamics and the spatiotemporal distributions of the accelerating E fields at the rear surface of the target are inferred from the detailed spectra.

DOI: 10.1103/PhysRevLett.89.085002 PACS numbers: 52.38.Kd, 41.75.Jv

For over 25 years, energetic protons and ions have been generated by focusing $\sim$ns pulses from large Nd:glass and CO_2 lasers ([1] and references therein) on solid targets at intensities of 10^{14}–10^{16} W/cm^2. The ions emerging from the coronal plasma are emitted into a large solid angle. They exhibit strong trajectory crossing and a broad energy spectrum with typical ion temperatures of $\sim$100 keV/nucleon. These unspectacular characteristics have prevented major applications. This scenario is totally different when the ion acceleration is caused by femtosecond (fs) laser pulses. When these are focused on thin foils targets (~ 50 μm) at intensities of $>10^{19}$ W/cm^2, proton beams are observed which exhibit new features [2–4]: (i) 10^{11}–10^{13} well collimated ($<20°$) protons with 5 to 50 MeV are generated, (ii) they come from the *rear surface* and move in the laser direction, and (iii) they form a dense, charge-neutralized bunch of $\sim$1 ps duration. These proton beams have already been applied for the diagnostic of high-density plasmas [5] and suggested for fast ignition [6]. Application in isotope production for positron emission tomography might follow soon.

Hatchett and Wilks [7,8] attribute the above mentioned characteristics of the proton beam to the so-called target-normal sheath acceleration mechanism (TNSA), the notion being that relativistic electrons with density, n_e, and temperature, T_e, created at the target front side penetrate the foil and by extending past the rear surface produce a strong space-charge field:

$$E \approx k_B T_e / e\lambda_D, \qquad \lambda_D = (\epsilon_0 k_B T_e / e^2 n_e)^{1/2}. \quad (1)$$

Typical values of $k_B T_e \sim 2$ MeV and $n_e \sim 2.5 \times 10^{19}\,\mathrm{cm}^{-3}$ yield $\lambda_D \sim 2$ μm (distance over which the electric field E decays) and $E > 10^{12}$ V/m. A few monolayers of atoms at the rear surface experience field ionization by barrier suppression (FIBS) [9] and are accelerated normal to the surface by E. The most energetic electrons always extend farther out into vacuum, maintaining the accelerating field as long as the electron temperature is high. This is fundamentally different from the long-pulse case, in which bulk effects and collisional ionization by thermal electrons in the coronal plasma are the dominant mechanisms. In the fs case, however, the ion generation and acceleration mechanisms are decoupled from the *stochastic* laser-plasma interaction, which offers many advantages for producing well-controlled ion beams. The decoupling and the rapid rear-surface acceleration are the reasons why the protons appear in a highly laminar, low emittance ps bunch inside which no trajectory crossing occurs. So far, mainly protons have been observed from the rear side. This is attributed to contaminations of hydrocarbon and H_2O layers adhered to the target. Because of its low ionization potential and high charge-to-mass ratio hydrogen is among the first ion species produced and most effectively accelerated, thereby screening the space-charge fields for all other ion species.

In this Letter, we present the first experimental study demonstrating that besides protons also high-brightness, high-energy ($\sim$ MeV/nucleon) ion beams can be accelerated from the *rear surface* of thin foils. These ions are effectively accelerated only if the hydrogenous surface contaminants are removed. We obtain absolutely calibrated high-resolution energy spectra of different ion species and charge states. These provide additional information, not in the proton signal, about the spatiotemporal evolution of the accelerating field and the origin of the observed ions. We show for the first time that it is possible to control the accelerated ion species by choosing a target composed of a front-side interaction material and a rear-side ion source layer. The high-energy ions out of these prepared source layers unambiguously prove the existence of an effective rear-surface acceleration mechanism. For our experimental conditions, we thereby resolve the long-standing

controversy as to whether the high-energy (> 10 MeV) protons come from the rear surface and are accelerated by the TNSA mechanism [6,10–12] or stem from the front surface and are accelerated by the charge-separation field in the laser plasma [3,13]. The electric field deduced from the ion spectra can explain the high-energy protons (> 25 MeV [4]) in our experiments. This result also constitutes a major difference to long-pulse experiments, where rear-surface acceleration was a minor effect only, that vanished almost completely when either the contaminating hydrocarbons were removed [14] or foils thicker than a few μm were used [15]. With the new capability to accelerate ion species at will and indications that beam focusing [4], spectra and charge state control might be feasible, applications such as laser accelerators are becoming realistic. Also the transport of a dense charge-neutralized ion beam in plasmas and solids, enabling isochoric heating of macroscopic volumes ($\sim 10^5$ μm^3) to > 300 eV, could now be studied.

Our experiments were performed with the 100-TW laser at the Laboratoire pour l'Utilisation des Lasers Intenses (LULI). The laser pulses (~ 30 J, ~ 300 fs, 1.05 μm) were focused at normal incidence on target to an intensity of up to 5×10^{19} W/cm^2. The contrast, i.e., the peak-to-pedestal intensity ratio, amounts to $\sim 10^7$ at $t = 1.5$ ns. As targets we used 50 μm thick Al and W foils coated on the rear side with 1 μm carbon or 0.3 μm CaF_2, respectively. The accelerated particles were investigated by three complementary diagnostics: (a) a stack of radiochromic films (RCF) 5 cm behind the target to record the angular distribution of the emitted proton beam [7,16], (b) a magnetic proton spectrometer [17] at 13° to the target normal with a Kodak DEF x-ray film to measure the proton energy spectra, and (c) two Thomson parabola spectrometers ($B = 0.65$ T, $E = 1.3$ MV/m) with CR-39 track detectors at 0° and 6° at a distance of about 1 m (solid angle $\sim 5 \cdot 10^{-8}$ sr) to obtain the ion energy spectra. CR-39 is sensitive to single ion events but insensitive to electromagnetic radiation and electrons. An ion striking a CR-39 plate destroys the polymer matrix along its path and causes nm-scale damage sites. These are transformed into cone- or bowl-shaped craters when the CR-39 is etched in NaOH solution. Each individual track is analyzed by optical microscopy with custom pattern recognition software [18] yielding position and track size parameters, from which the absolute ion energy spectra are then obtained. Because the optical density is not simply proportional to the number of pits, only ''single-track counting'' yields correct results for the areal ion density, whereas optical scanning may lead to erroneous results.

To remove the hydrogenous contaminants, we tried radiative, laser, and resistive heating and found the latter the most effective (see also [19]). We heated Al and W foils up to ~ 600 K and ~ 1200 K, respectively. Already the partial removal of hydrocarbons strongly enhanced the acceleration of carbon ions, as shown in Fig. 1. The proton spectrometer yielded typically $\sim 10^{11}$ protons of up to 25 MeV, for unheated targets. For heated Al targets, the number of protons is reduced to $\sim 10^{10}$ with energies of up to 3 MeV. The energy of the carbon ions is increased by a factor of ~ 2.5 and the number by 2 orders of magnitude to $\sim 2 \times 10^{11}$, corresponding to a laser-to-ion energy conversion of 0.5%. Acceleration is most efficient for C^{4+} ions, with a cutoff energy of ~ 1 MeV/nucleon at the high-energy end. In all spectra the high-energy cutoff is dependent on the charge state, ruling out recombination as a dominant effect in our experiments. This is confirmed by the low number of neutral atoms ($\sim 1\%$) forming the pinhole image on the CR-39. This behavior is fundamentally different from that observed in the carbon spectra in long-pulse experiments [20], where all charge states had a similar cutoff and the *rear-surface* ion signal almost vanished for heated targets [19]. Using W targets, the higher heating temperatures resulted in a complete removal of hydrocarbons. The proton spectrometer as well as the CR-39 did not show any protons, while strong fluorine ion tracks are observed originating from the CaF_2 layer at the target rear side (Fig. 2). Since only the target rear surface is coated with either C or CaF_2, the carbon and fluorine ions originate unambiguously from the *rear surface* of the targets. The acceleration of heavier ions was again increased considerably: F^{7+} was accelerated up to 100 MeV (> 5 MeV/nucleon) at $> 5\%$ energy conversion. The RCF confirmed this by showing a narrow spot in the first layer, which, in the absence of protons, indicates fluorine ions of energies above 4 MeV/nucleon. The analysis of the lower charge states

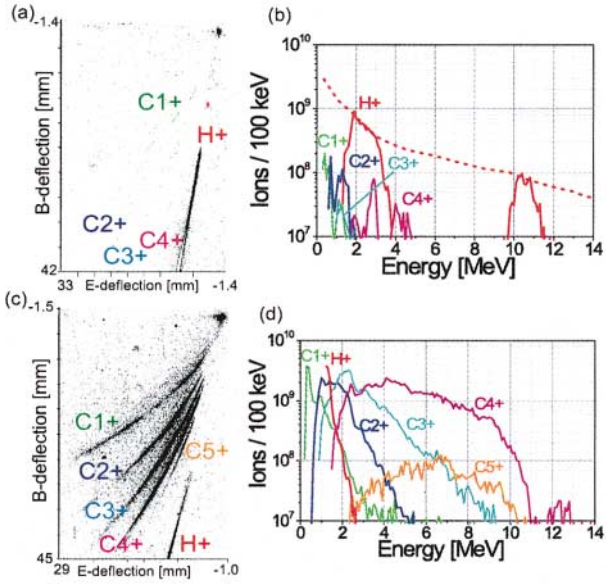

FIG. 1 (color). (a) Ion traces (on CR39) from an unheated Al | C target and (b) corresponding spectra. The gap in the proton signal is due to the CR-39 detector which is optimized for heavier particles. The dotted line illustrates the H^+ spectra as obtained with the proton spectrometer. (c) Ion traces from a heated Al | C target and (d) corresponding spectra. The ion signals are strongly enhanced. The spot in the upper right corner of (a),(c) is the pinhole image formed by neutral atoms.

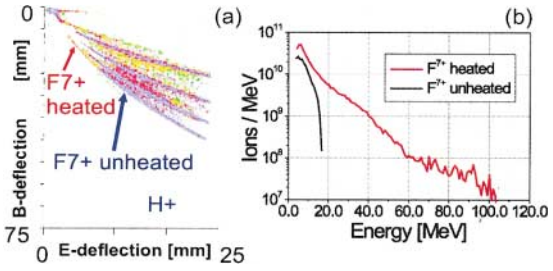

FIG. 2 (color). (a) Overlayed signals of heated (orange) and unheated (blue) W | CaF_2 targets: The proton signal vanishes for heated targets; the fluorine signals (especially F^{7+}) go up to much higher energies. (b) Corresponding F^{7+} spectra: F^{7+} ions achieve more than 100 MeV (5 MeV/nucleon).

proves to be more difficult due to overlapping of F and Ca traces with similar charge-to-mass ratios.

Long-pulse experiments showed that ion spectra can be used to identify the ionization and acceleration mechanisms, e.g., isothermal expansion (with $T_{e,\mathrm{hot}} \sim$ 10–100 keV) and collisional ionization up to the highest charge state (e.g., C^{6+}), followed by recombination to the lower charge states in the drift phase ([1,20] and references therein). In short-pulse experiments, however, FIBS in the strong transient space-charge field dominates because of the fs timescale and high electron temperature ($\sim$ MeV). We can rule out ionization by the laser pulse or by a shock front by simultaneous target interferometry. The laser pulse is completely absorbed in the preplasma and the target thickness is chosen to prevent prepulse-caused shock breakout until $\sim$10 ns after the main pulse. Collisional ionization is estimated from [21]:

$$\nu_{\mathrm{col}} \approx n_e v_e 4\pi a_b^2 (U_H^2/U_k k_B T_e) \ln(k_B T_e/U_k), \tag{2}$$

where a_b is the Bohr radius, v_e is the electron velocity, and U_k and U_H are the ionization potentials of the ionized species and hydrogen, respectively. We also considered the influence of heating by possible return currents with a temperature $k_B T_e^{\mathrm{ret}} \sim 50$ eV [22], which must balance the hot electron flow, i.e., $n_e^{\mathrm{ret}} v_e^{\mathrm{ret}} \simeq n_e^{\mathrm{hot}} v_e^{\mathrm{hot}} \Rightarrow n_e^{\mathrm{ret}} \sim 2.5 \times 10^{21}\,\mathrm{cm}^{-3}$. We estimated the field ionization rate from the ADK model [23]:

$$\nu_{\mathrm{ADK}} \approx 6.6 \cdot 10^{16} (Z^2/n_{ef}^{4.5}) \exp[-(2Z^3/3n_{ef}^3)(E_{\mathrm{at}}/E)][10.87(Z^3/n_{ef}^4)(E_{\mathrm{at}}/E)]^{2n_{ef}-1.5}, \tag{3}$$

where $E = 2$ TV/m [from Eq. (1)] is the ionizing field, $E_{\mathrm{at}} = 0.51$ TV/m is the atomic electric field, Z is the charge of the created ion, and $n_{ef} = Z/\sqrt{U_k/U_H}$. The various ionization frequencies are listed in Table I. Other analytical models yield similar results and the exact numerical rates are even higher [23]. For all models field ionization dominates by orders of magnitude over the collisional processes for our set of parameters and for charge states up to He-like. For C^{5+}, $\nu_{\mathrm{col}}^{\mathrm{hot}}$ is larger than ν_{ADK}, which may explain the different spectral shape and lower numbers for this charge state. Assuming detailed balancing [24], we estimate recombination rates of $\sim$1% consistent with our measured data.

Having established that the ion spectra are linked to the accelerating E fields, we can now extract information such as the field strength which is not available from the proton data. With FIBS as the dominant ionization process, the $k+$ -ionic state will be created as soon as the electric field is above the threshold

$$E_k = U_k^2 \varepsilon_0 \pi / eZ. \tag{4}$$

We can use E_{k+1} as an upper limit for the electric field strength that a $k+$ ion has experienced. By integrating the equations of motion for an ion in a field rising in time with the laser pulse to E_k, staying at this value for a time τ_k^{min} and then decaying exponentially, τ_k^{min} defines a lower limit for the acceleration time, required to achieve the observed maximum ion energy for a given charge state (see Table I). The acceleration length, l_k^{min}, is the distance traveled by an ion during τ_k^{min} and is therefore a measure for the minimal spatial extension of the fields. The ultra-high-field region turns out to be of the duration of the laser pulse and of short length (≤ 500 fs, ≤ 5 μm). Only the C^{4+} ions see these

TABLE I. Calculated field and ionization parameters for carbon. U_k is the ionization potential of the kth ionic charge state and E_k is the corresponding field strength [Eq. (4)]. E_k^{max} is the maximal E field, τ_k^{min} is the minimal field duration, and l_k^{min} is the minimal acceleration length for a given k. ν are the ionization frequencies due to the hot electrons ($k_B T_e^{\mathrm{hot}} \sim 2$ MeV, $n_e^{\mathrm{hot}} \sim 2.5 \times 10^{19}$ cm^{-3}), the return current ($k_B T_e^{\mathrm{ret}} \sim 50$ eV, $n_e^{\mathrm{ret}} \sim 2.5 \times 10^{21}$ cm^{-3}), and the field ionization ($E_f = 2$ TV/m). Because $\tau_4^{\mathrm{min}} \sim \tau_{\mathrm{laser}}$, E_4^{max} is lower than the theoretically possible value of $5.3 \cdot 10^{12}$ V/m.

k	U_k (eV)	E_k (V/m)	E_k^{max} (V/m)	τ_k^{min} (ps)	l_k^{min} (μm)	$\nu_{\mathrm{col}}^{\mathrm{hot}}$ (ps^{-1})	$\nu_{\mathrm{col}}^{\mathrm{ret}}$ (ps^{-1})	ν_{ADK} (ps^{-1})
1	11.2	2.2×10^{10}	5.2×10^{10}	60	230	2.53×10^{-2}	2.13	5.93×10^{4}
2	24.4	5.2×10^{10}	1.3×10^{11}	10	48	1.1×10^{-2}	0.68	2.65×10^{5}
3	47.9	1.3×10^{11}	1.8×10^{11}	4.3	25	5.29×10^{-3}	0.21	1.46×10^{6}
4	64.5	1.8×10^{11}	1.75×10^{12}	0.35	3	3.28×10^{-3}	0.11	4.62×10^{6}
5	392	5.3×10^{12}				5.29×10^{-4}	$\cdots$	8.5×10^{-5}
6	490	7.0×10^{12}				4.14×10^{-4}	$\cdots$	7.03×10^{-9}

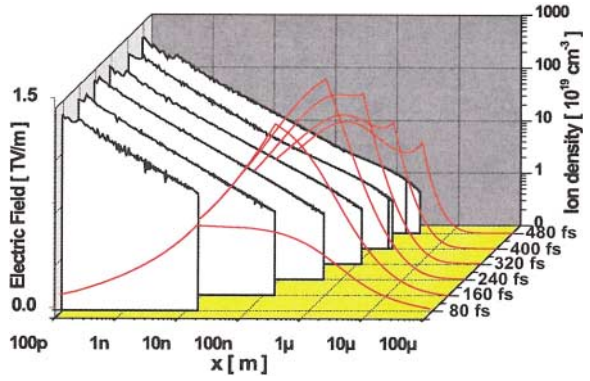

FIG. 3 (color). Space-time history of the accelerating electric fields (red curves) and the C^{4+}-dominated ion distributions (white curves) as calculated by our model: The field maximum moves out into the vacuum. Already during the pulse there exists an ion distribution on a μm scale.

highest fields, while the lower charge states are accelerated by lower fields of up to 2 orders of magnitude longer duration, which is not explainable by the static TNSA model.

In order to get a better understanding of how the ion energies and charge state distributions develop in space and time, we have developed a 1D-numerical model which calculates the electron dynamics behind the target, assuming a Boltzmann equilibrium for the electron energy spectrum and a current distribution which follows the laser pulse. We include the ionization process (FIBS), the acceleration of different ion species, and screening effects on the potential. In each time step, we solve Poisson's equation for the given charge distribution, check for ionization events, advance the different ion species, and solve again Poisson's equation for the new charge distribution. When the first laser-heated electrons enter the vacuum behind the target, they create the space-charge field E, albeit in a highly dynamic way, much more complex than in the simple TNSA model. When more and hotter electrons pass through the surface, the field increases until $E = E_1$. Now FIBS sets in and the produced ions and electrons decrease the field at the surface. An equilibrium between the growing external field and the surface ionization rate keeps the field at the surface always at E_1. The created ions are accelerated into the vacuum while the freed electrons are pushed into the target. Whereas the field close to the target is shielded by the ions, the unshielded field in vacuum keeps increasing. The maximum of the electric field moves outwards into vacuum, ionizing the outermost ions further (see Fig. 3). The model reproduces the measurements for protons and the high charge states. As long as there is a source of hot electrons, nearly all ions are sequentially ionized to C^{4+}. As seen in the experimental data, the lower charge states require 2 orders of magnitude longer time scales and possibly a 3D treatment to allow for low fields in the fringe regions. To explain the long acceleration times the electron recirculation model of [10] may prove useful. Another approach is to envision the individual charge states in separately lined up bunches each with a charge neutralizing electron cloud lagging a bit behind, thereby setting up an effective field for the next lower charge state bunch. A model to completely explain the acceleration dynamics is currently developed. The evaluation of the fluorine shot shown in Fig. 2 shows that $E \sim 2$ TV/m active over $\tau_7^{\min} \sim 350$ fs is necessary to accelerate F^{7+} ions up to 100 MeV over a scale length of $l \sim 10$ μm. The inferred fields would accelerate H^+ up to ~ 25 MeV, as typically observed with unheated targets.

In summary, by using high-intensity laser pulses we achieved efficient ($> 5\%$ energy conversion), directed ion acceleration to more than 5 MeV/nucleon from the *rear surface* of thin-foil targets. High-resolution energy spectra measured for different ionic charge states yield detailed information on the spatiotemporal behavior of the accelerating fields. They show that FIBS is the dominant ionization mechanism while recombination and collisional ionization are negligible except for C^{5+}. A 3D-TNSA model including dynamic fields and multiple ion species is needed to correctly describe the acceleration process.

We thank A. Kemp and H. Ruhl for fruitful discussions and the LULI-laser team for their support. LULI is UMR 7605, CNRS-CEA-Université Paris VI École Polytechnique. This work was supported by EU Programme No. HPRI CT 1999-0052, by Grant No. E 1127 from Région Ile-de-France, and by corporate support from GA.

[1] S. Gitomer *et al.*, Phys Fluids **29**, 2679 (1986).
[2] R. Snavely *et al.*, Phys. Rev. Lett. **85**, 2945 (2000).
[3] E. Clark *et al.*, Phys. Rev. Lett. **84**, 670 (2000).
[4] M. Roth *et al.*, Phys. Rev. ST Accel. Beams **5**, 061301 (2002).
[5] M. Borghesi *et al.*, Phys. Rev. Lett. **88**, 135002 (2002).
[6] M. Roth *et al.*, Phys. Rev. Lett. **86**, 436 (2001).
[7] S. Hatchett *et al.*, Phys. Plasmas **7**, 2076 (2000).
[8] S. Wilks *et al.*, Phys. Plasmas **8**, 542 (2001).
[9] S. Augst *et al.*, J. Opt. Soc. Am. B **8**, 858 (1991).
[10] A. Mackinnon *et al.*, Phys. Rev. Lett. **88**, 215006 (2002).
[11] Y. Murakami *et al.*, Phys. Plasmas **8**, 4138 (2001).
[12] A. Mackinnon *et al.*, Phys. Rev. Lett. **86**, 1769 (2001).
[13] A. Maksimchuk *et al.*, Phys. Rev. Lett. **84**, 4108 (2000).
[14] F. Begay *et al.*, Phys. Fluids **25**, 1675 (1982).
[15] G. Tsakiris *et al.*, Phys. Rev. Lett. **46**, 1202 (1981).
[16] E. Clark *et al.*, Phys. Rev. Lett. **85**, 1654 (2000).
[17] T. Cowan *et al.*, Phys. Rev. Lett. **84**, 903 (2000).
[18] G. Rusch *et al.*, Nucl. Tracks Radiat. Meas. **19**, 261 (1991).
[19] F. Begay *et al.*, J. Phys. D **13**, L29 (1980).
[20] C. Joshi *et al.*, Appl. Phys. Lett. **34**, 625 (1979).
[21] V. Tikhonchuk, Phys. Plasmas **9**, 1416 (2002).
[22] L. Grémillet *et al.*, Phys. Rev. Lett. **83**, 5015 (1999).
[23] D. Bauer *et al.*, Phys. Rev. Lett. **75**, 4622 (1995).
[24] L. Oster, Am. J. Phys. **38**, 754 (1970).